

X-ray mapping the outer regions of galaxy clusters at $z=0.23$ and 0.45

Q. Daniel Wang^{1,2,*} and Stephen Walker²

¹*Department of Astronomy, University of Massachusetts, Amherst, MA 01003, USA*

²*Institute of Astronomy, University of Cambridge, Madingley Road, Cambridge CB3 0HA, UK.*

27 January 2014

ABSTRACT

The thermal, chemical, and kinematic properties of the potentially multi-phase circum/intergalactic medium at the virial radii of galaxy clusters remain largely uncertain. We present an X-ray study of Abell 2246 and GMBCG J255.34805+64.23661 ($z = 0.23$ and 0.45), two foreground clusters of the UV-bright QSO HS 1700+6416, based on 240 ks *Chandra*/ACIS-I observations. We detect enhanced diffuse X-ray emission to the projected distances beyond r_{200} radii of these two clusters. The large-scale X-ray emission is consistent with being azimuthally symmetric at the projected radii of the QSO (0.36 and 0.8 times the radii of the two clusters). Assuming a spherical symmetry, we obtain the de-projected temperature and density profiles of the X-ray-emitting gas. Excluding the cool cores that are detected, we find that the mean temperature of the hot gas is ~ 4.0 keV for Abell 2246 and 5.5 keV for GMBCG J255.34805+64.23661, although there are indications for temperature drop at large radii. From these results, we can estimate the density and pressure distributions of the hot gas along the QSO sightline. We further infer the radial entropy profile of Abell 2246 and compare it with the one expected from purely gravitational hierarchical structure formation. This comparison shows that the ICM in the outer region of the clusters is likely in a clumpy and multi-phased state. These results, together with the upcoming *HST*/COS observations of the QSO sightline, will enable a comprehensive investigation of the multi-phase medium associated with the clusters.

Key words: galaxies: clusters: general, galaxies: clusters: individual: Abell 2246 GMBCG J255.34805+64.23661, X-rays: galaxies: clusters

1 INTRODUCTION

A major recent advance in the study of nearby galaxy clusters is the detection of apparently diffuse X-ray emission from their outer regions at radius $r \sim r_{500} - r_{200}$, where r_{200} (or r_{500}) is the radius within which the mean mass density is 200 (or 500) times the critical density of the universe at the redshift of a cluster (e.g., George et al. 2009; Hoshino et al. 2010; Simionescu et al. 2011; Eckert et al. 2012; Walker et al. 2013). In particular, there is now strong evidence for the inhomogeneous distribution of the intra-cluster medium (ICM) in these regions. This inhomogeneous and hence potentially multi-phase nature of the ICM is expected from simulations of the structure formation of the universe, which show a complicated shock heating/cooling history of the ICM in regions near the virial shock, typically located at $r \sim r_{200}$ of a cluster (e.g., Roncarelli et al. 2006; Molnar et al. 2009). The clustering environment can also strongly affect the circumgalactic medium (CGM) of individual galaxies, via such processes as ram-pressure stripping

and pressure compression (e.g., Yoon & Putman 2013; Lu & Wang 2011). Understanding these phenomena and physical processes is clearly important, not only for determining the content and state of the baryon matter in the outer regions of clusters, but for their utility as cosmology probes as well (e.g., via the observations of the Sunyaev-Zel’dovich effect; Carlstrom, Holder & Reese 2002).

However, it has been challenging for existing studies to cover the large angular extents of nearby clusters and to calibrate out various systematics, which are important for mapping out the low surface intensity of the X-ray emission. Indeed, much of the advance has been made, largely because of the extensive observations made with *Suzaku*/XIS, which has a low instrumental background. But, the studies are fundamentally limited by various uncertainties, such as the cosmic variance (in the surface density of discrete and extended X-ray sources due to the structured nature of the universe; Hickox & Markevitch 2006), the intensity and spectral variation of the Galactic soft X-ray foreground across large sky areas and the time-dependent contributions from solar wind charge exchanges in the earth’s magnetosphere and/or the heliosphere (Koutroumpa et al. 2006).

* E-mail: wqd@astro.umass.edu

Complementary investigations can be conducted with deep *Chandra* observations of distant clusters ($z \gtrsim 0.2$). The superb spatial resolution and sensitivity of such observations allow for the mapping of the X-ray emission from clusters with minimal confusion from spurious sources and little differential foreground variation. In a single observation (especially with the ACIS-I at the aim point), both a cluster and its local sky background can be covered. In addition to these advantages, such investigations are, of course, essential to the understanding of the galaxy cluster building process across the cosmic time. Bonamente et al. (2013) have reported the first *Chandra* detection of diffuse X-ray emission out to the virial radius of the cluster Abell 1835 at $z = 0.253$. A sharp drop in temperature is detected at large radii, indicating that the ICM there is significantly clumped and/or contains multiple phases.

Here we present a study of two intermediate redshift clusters, Abell 2246 and GMBCG J255.34805+64.23661 (Clusters A and B hereafter; Table 1) based on nine *Chandra* observations of a total 240 ks exposure. The X-ray emission from these two clusters (Fig. 1), are serendipitously discovered by *ROSAT* observations of QSO HS 1700+6416 ($z = 2.72$; Reimers et al. 1997; Just et al. 2007; Lanzuisi et al. 2012). This QSO is $2.2'$ and $3.2'$ off the center of Cluster A and B, respectively. These QSO/cluster alignments, well within the projected virial radii of the clusters (Fig. 1; see § 3) allow for various absorption line studies, especially at far-UV with upcoming *HST/COS* observations, which will be sensitive to OVI doublet (1032 and 1037 Å), HI Ly- α and Ly- β , as well as many other transitions. These lines can offer unique information about the thermal, kinematic, and/or chemical properties of cold and warm gases. The combination of such a multi-wavelength studies will enable us to probe all phases of the ICM, as well as the CGM associated with individual galaxies, at multiple impact radii. The early *Chandra* observation, OBS# 547 (Table 2), has been included in various X-ray surveys of clusters (e.g., Maughan et al. 2008; Ettori & Balestra 2009). The other eight observations have been used to investigate a $z = 2.30$ protocluster in the field (Digby-North et al. 2010). While the diffuse X-ray emission from this protocluster is not detected, two discrete X-ray sources are identified as the counterparts of emission line AGNs in this protocluster.

The focus of the present paper is on Clusters A and B. We use the nine observations together to characterize the properties of the hot ICM of the clusters along the QSO sightline, as well as their global X-ray structures. We describe the nine observations and our reduction of the data in § 2, present our data analysis in § 3, and infer the radial properties of the ICM in § 4. In § 5, we summarize our results and discuss their implications and expected synergy with the UV absorption line spectroscopy. We use the standard Λ CDM cosmology and present the error bars of our measurements at the 68% statistical confidence level, unless noted otherwise.

2 OBSERVATIONS AND DATA REDUCTION

The *Chandra* data used in the present work were taken in nine separate observations (Table 1). We reprocess the data with the latest version of the *Chandra* Interactive Analysis of Observations (CIAO; version 4.5). We remove time intervals of significant background flares with count rates deviating more than 3σ or a factor of $\gtrsim 1.2$ from the mean rate of individual observations, using Maxim Markevitch's light-curve cleaning routine LC_CLEAN. This cleaning, together with a correction for the dead time of the observations, resulted in a total 239.5 ks exposure for subsequent analysis.

OBS 547 was taken in 2000, about seven years earlier than the rest of the observations, which were all within a period of 10 days and with the essentially same pointing positions and roll angles. Both the instrument response and the non-X-ray background level were significantly different between these two time periods. Thus OBS 547, also with a pointing offset of $\sim 5.6'$ from the rest, is dealt with separately, in both imaging and spectral analyses. This offset between the two data sets allows us to test the sensitivity of our various measurements on the detector coverage and source detection sensitivity. We repeat the measurements such as radial X-ray intensity distributions by using the two data sets separately to test the consistency. Based on such tests, for example, we decide to avoid the use of the regions with effective exposures $\lesssim 20$ ks in our quantitative measurements to minimize the effects of low counting statistics and the incomplete mapping of the field, mostly in its outermost edges.

We estimate non-X-ray background contributions, using the ACIS stowed background database (Group “D” for OBS# 547 and “E” for the rest). The charge-transfer inefficiency and gain corrections of the database are all matched to those of the present observations. Both the data and background events are cleaned for the VFaint data mode. The stowed background level in each observation is further normalized according to the rates in the 9–12 keV band, where events are almost completely due to the non-X-ray background.

We construct effective exposure maps in the four bands: 0.5–1 (S1), 1–2 (S2), 2–4 (H1), and 4–8 (H2) keV. The construction of these broad-band exposure maps assumes a power law spectrum of photon index 1.7 and accounts for the telescope vignetting and bad pixels as well as the quantum efficiency variation of the instrument, including the time-dependent sensitivity degradation, which is particularly important at energies $\lesssim 1$ keV.

3 ANALYSIS AND RESULTS

Fig. 1a presents an overview of our interested field in the ACIS-I B (0.5–8 keV) band. This presented image is the sum of two intensity images constructed in the S (0.5–2 keV) and H (2–8 keV) bands and adaptively smoothed with the CIAO routine CSMOOTH. The smoothing scales are calculated separately in the two bands and with the S/N ratio ~ 3 . However, our quantitative analysis of the clusters is always based on the unsmoothed count, background, and exposure maps. We describe our detection of discrete X-ray sources in Appendix A. These sources are marked in Fig. 1a. Depending on the spectrum of a source, it may appear significant in the S or H band, sometimes not in the B band. This band-dependence of the X-ray emission can be better appreciated in the composite image presented in Fig. 1b.

3.1 Imaging analysis of the diffuse X-ray emission

We map out the diffuse X-ray emission in the field by exercising the sources in the count, background, and exposure maps. We remove a region of twice the 70% energy-encircled radius of the point spread function around each source. The X-ray intensities in these removed regions are interpolated from the surrounding areas in the smoothing process of the images. We use CSMOOTH with the Gaussian scale calculated adaptively to achieve a non-X-ray background-subtracted S/N ratio $\gtrsim 4$ for the count image in the S (0.5–2 keV) band. The same scale map is used to smooth the count, background, and exposure maps in the 0.5–1 keV and 1–2

Table 1. *Chandra* ACIS-I Observations

OBS#	R.A. (J2000) (h m s)	Dec. (J2000) (° ' ")	Exposure (s)	Roll Angle (°)	OBS Date (yyyy-mm-dd)
547	17 01 46.14	+64 12 04.3	46967	322.4	2000-10-31
8032	17 00 55.04	+64 11 26.7	30996	338.0	2007-11-12
8033	17 00 55.05	+64 11 26.7	29707	338.0	2007-11-20
9756	17 00 55.05	+64 11 26.7	31234	338.0	2007-11-14
9757	17 00 55.03	+64 11 26.7	20527	338.0	2007-11-13
9758	17 00 55.05	+64 11 26.6	23114	338.0	2007-11-16
9759	17 00 55.03	+64 11 26.7	31187	338.0	2007-11-17
9760	17 00 55.06	+64 11 26.7	16694	338.0	2007-11-19
9767	17 00 55.02	+64 11 27.0	9039	338.0	2007-11-21

The exposure represents the livetime (dead time corrected) of the cleaned data.

Table 2. Key parameters of the clusters

Cluster	A	B
Name	Abell 2246	GMBCG J255.34805+64.23661
Redshift	0.23	0.45
Center position	$17^h00^m41.8^s, +64^\circ12'59''$	$17^h01^m23.5^s, +64^\circ14'12''$
$L_{0.5-8 \text{ keV}} (\text{erg s}^{-1})$	1.9×10^{44}	5.4×10^{44}
Temperature (K)	$4.0^{+0.2}_{-0.3}$	$5.5^{+0.4}_{-0.4}$
$M_{200} (10^{14} M_\odot)$	$3.3^{+0.6}_{-0.4}$	$5.0^{+0.8}_{-0.7}$
$r_{200} (')/\text{Mpc}$	$6.1^{+0.5}_{-0.3}/1.3^{+0.1}_{-0.1}$	$4.0^{+0.2}_{-0.2}/1.4^{+0.1}_{-0.1}$
$I_0 (\text{cts s}^{-1} \text{ arcmin}^{-2})$	0.21	0.42
r_c/r_{200}	0.026	0.016
β	0.51	0.45
$\chi^2/d.o.f.$	79/36	46/36
QSO Impact parameter	2.2'	3.2'
$N_e (10^{20} \text{ cm}^{-2})$	6.5	4.0

Note: For each of the two cluster, the name and redshift are from NED, position from the present *Chandra* source detection, X-ray luminosity and temperature from the best-fit to the spectrum extracted from the region roughly within the projected r_{500} , the cluster mass (M_{200}) and r_{200} from their scaling relations with the temperature (Arnaud, Pointecouteau & Pratt 2005), β -model parameters (central count rate I_0 , projected core radius r_c , and β ; see Eq. 1) from the best-fit to the 0.5-2 keV intensity profile, electron column density N_e at the projected radius of HS 1700+6416.

keV bands. These smoothed images in each band are then used to construct a background-subtracted intensity map. The resultant maps in the two bands are added to form the final map in the S band, which is presented in Fig. 2.

The X-ray intensity of the clusters peaks at two optically red elliptical galaxies (SDSS J170041.75+641258.7 and J170123.53+641411.7; Figs. 3 and 4), both of which are detected as X-ray sources (#65 or J170041.75+641258.8 and #126 or J170123.46+641411.9; Table A1). The X-ray morphology of Cluster A is round and shows no significant substructure, indicating that the ICM is rather relaxed. By contrast, the inner region of Cluster B shows a strongly elongated X-ray morphology, which is lopsided toward to the northwest (Fig. 3), as is clearly seen in the close-up presented in Fig. 4. On the opposite side of this direction is another giant elliptical (SDSS J170128.23+641354.8). Thus this X-ray substructure most likely represents a recent subcluster merger. On larger scales ($r \gtrsim 1'$), the X-ray morphology appears relaxed.

Clearly, there is a projected overlap between the X-ray emissions from the two clusters. But this overlap is significant only in

a limited region. As illustrated in Fig. 5, this region, viewed from the center of one cluster, is mostly within $\pm 45^\circ$ about the direction toward the center of the other cluster. Excluding this angular interval, the azimuthal intensity distribution is consistent with a constant (i.e., this null hypothesis cannot be rejected at $\gtrsim 2\sigma$), at least at the projected radius of HS 1700+6416 in each cluster. At larger radii, the azimuthal intensity distribution shows a greater dispersion. This may indicate an increasing clumpiness of the intensity distribution with the increasing radius. But much of the dispersion can be attributed to the cosmic variance of the background/foreground emission (mostly due to the projected large-scale structure variation from one field to another). Indeed, the local background fields (Fig. 2b) show comparable intensity dispersions. Therefore, our detailed analysis in the following is focused on the integrated or azimuthally-averaged radial properties of the clusters.

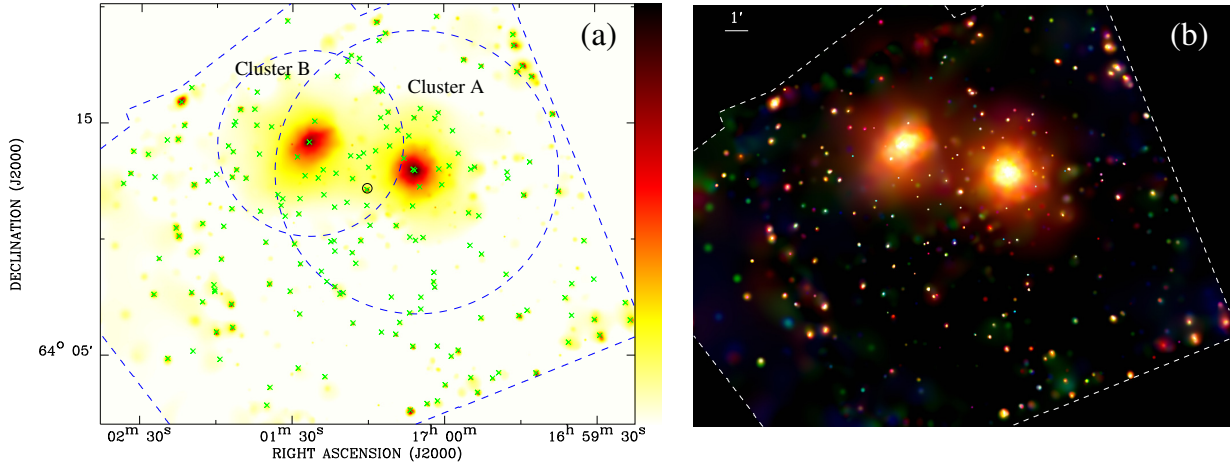


Figure 1. X-ray intensity images of our studied field in various ACIS-I bands. (a) Image in the B (0.5-8 keV) band. The positions of the detected sources are marked with crosses, whereas HS 1700+6416 is highlighted by a small circle. (b) Tri-color montage of X-ray intensities in the same field: (red) 0.5-2 keV, (green) 2-4 keV, and (blue) 4-8 keV. The dashed contour outlines the boundaries of the field covered by the merged ACIS-I data, while the large circles mark the r_{200} radii of the clusters.

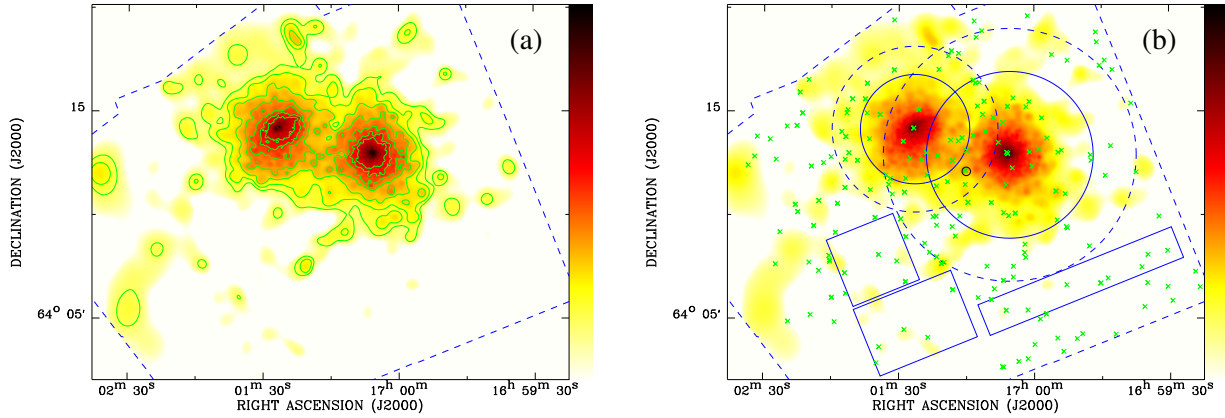


Figure 2. Diffuse 0.5-2 keV emission intensity map of the field: (a) The contours (in units of 10^{-4} cts s^{-1} arcmin $^{-2}$) are at 4.5, 6, 9, 15, 27, 51, and 99; the lowest level is about 3σ above the local sky background of an intensity ~ 3 ; (b) The same image as in (a), but with the outlines of the spectral extraction regions for the two on-cluster regions (solid circles) and three off-cluster background regions (solid boxes). The rest is the same as in Fig. 1.

3.2 Spectral analysis of the diffuse X-ray emission

ACIS-I spectra are extracted in concentric annuli, centered on the peaks of the X-ray emission of each cluster (Fig. 2b). The radii of these annuli are determined so that each contains at least 1000 counts following the non-X-ray background subtraction. When performing the spectral extraction for each cluster, the overlapping region with the other cluster is excluded. The ARFs and RMFs are created for each extracted spectrum using the CIAO routines MKWARF and MKACISRMF, allowing us to account for the variation in the effective area across the chip. The spectral analysis uses the software packages XSPEC (version 12.8).

The local sky background is estimated in the regions chosen to be well away from the extended emission of the two clusters. After the non-X-ray background is subtracted in XSPEC, the ACIS-I spectrum of the local sky X-ray background is mod-

eled as the sum of the extragalactic contribution and a Galactic foreground. The latter is characterized with two optically-thin thermal plasma (APEC) components: an unabsorbed one at $kT = 0.14$ keV for the Local Hot Bubble and an absorbed one at $kT = 0.6$ keV, representing the Galactic halo emission. The temperatures of these components are found by fitting to the *ROSAT* all-sky survey spectrum for an annulus around the two clusters (between 0.5-1.0 degrees). (The survey data are obtained from the X-ray background tool at <http://heasarc.gsfc.nasa.gov/cgi-bin/Tools/xraybg/xraybg.pl>.) The extragalactic contribution from unresolved point sources is modeled as a power law of index 1.4. The fit to the ACIS-I spectrum then determines the normalizations of the combined thermal component and the power law. The best-fit model is then included in the analysis of the non-X-ray-subtracted on-cluster spectra, accounting for their geometrical area differences

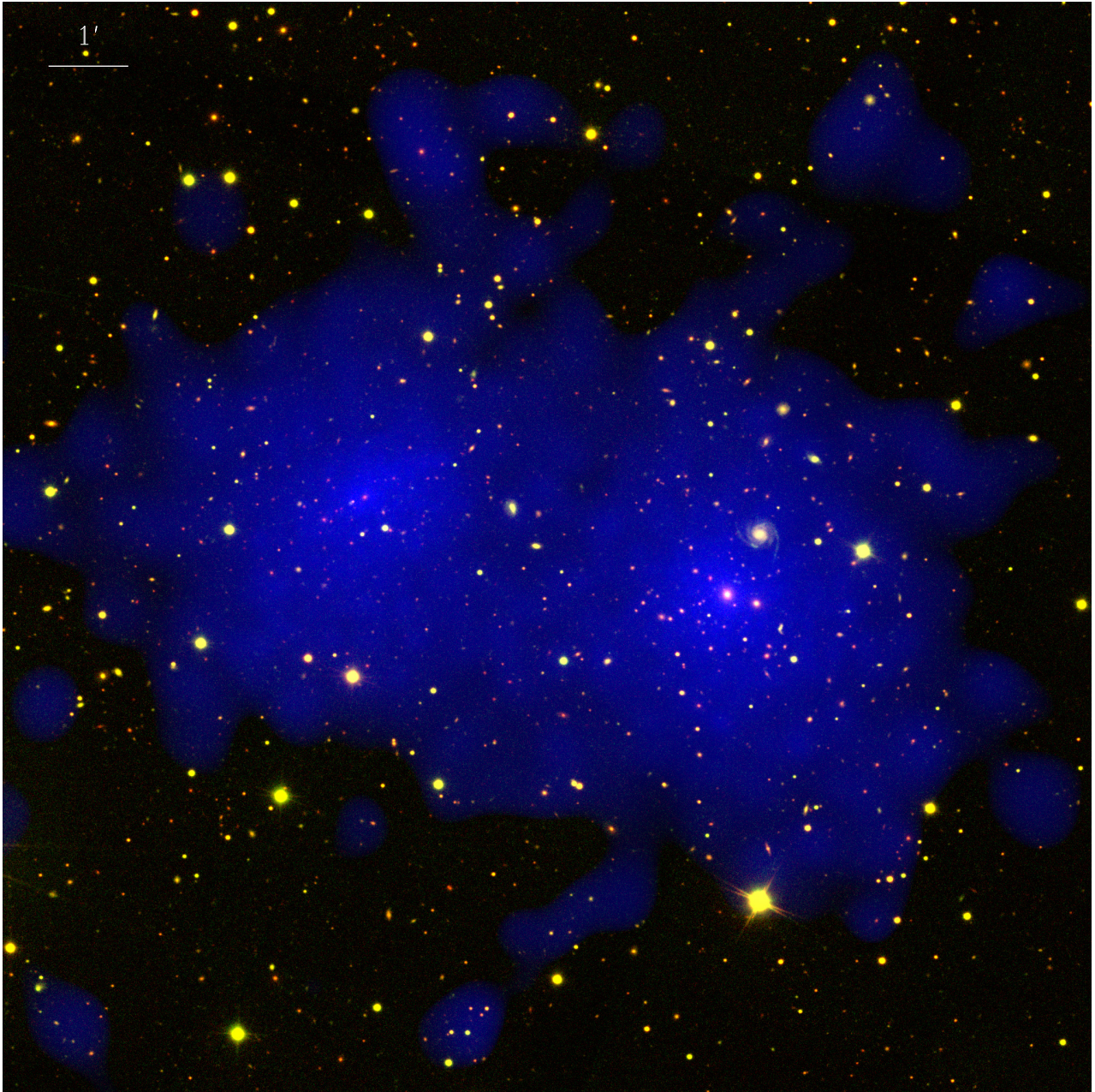


Figure 3. Multi-wavelength montage of the two cluster field: SDSS r (red) and g (green) bands, as well as 0.5-8 keV diffuse X-ray emission (blue).

from the local background region and assuming that the spectral shape and surface brightness of the sky X-ray background remain the same across the *Chandra* field of the present study.

This double-subtraction method of the background contributions accounts for the variation of the X-ray effective area across the field, as well as the potential change of the non-X-ray background across the detector. If one simply subtracted the *observed* spectrum in the background region (near the edge of the ACIS-I field of view) from the cluster emission regions (which are closer to the axis of the observations), the background would be underestimated because the effective area is lower off axis.

Due to the low counting statistics of the spectral channels, we use the extended C-statistic when performing the spectral fits. The column density is fixed to the Leiden/Argentine/Bonn survey value of $2.2 \times 10^{20} \text{ cm}^{-2}$ (Kalberla et al. 2005), and the redshift is also

fixed to the value of each cluster. The temperature, metal abundance, and normalization of the APEC component are allowed to be free parameters, and the profiles of temperature and metallicity are shown in Fig. 6. The metal abundance is relative to the solar one given by Anders & Grevesse (1989).

The cool cores of the two clusters are resolved. The metallicity peaks at the cores. With the core bins excluded, we find the average temperatures as listed in Table 2, although there is marginal evidence for declining temperature with increasing radius for Cluster A.

From the average temperatures, we estimate M_{200} and r_{200} , using the scaling relations of Arnaud, Pointecouteau & Pratt (2005): $h(z)M_{200} = 5.34 M_{\odot} (kT/5 \text{ keV})^{1.72} 10^{14}$, and $h(z)r_{200} = 1674 \text{ kpc} (kT/5 \text{ keV})^{0.57}$. Folded through these estimates are the statistical uncertainties in the temperatures and in the scaling re-

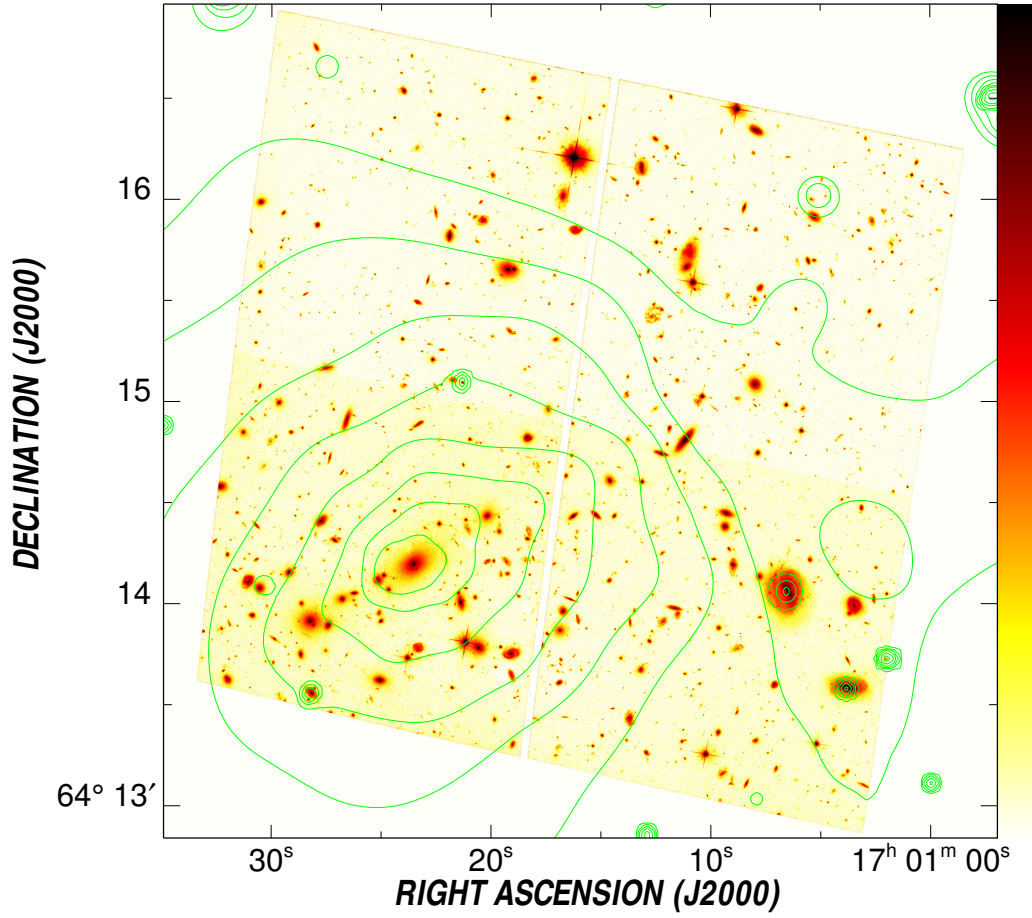


Figure 4. Close-up of the inner region of Cluster B. Overlaid on the false color image of the *HST* optical images (ACS/WFC F814W filter) are the intensity contours of the 0.5-8 keV band emission at 0.5, 1, 2, 4, 8, 16, 32, and 64 above a local background of 1.5 (all in units of 10^{-4} cts s^{-1} arcmin $^{-2}$).

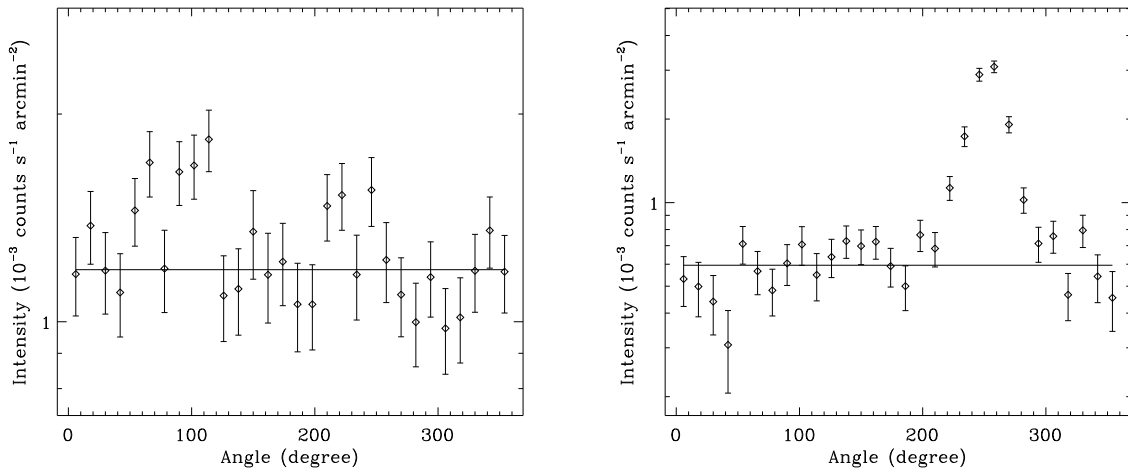


Figure 5. Azimuthal distributions of the diffuse X-ray intensity of Clusters A (left panel) and B (right) in the 0.5-2 keV band. For each cluster, the data used for the distribution calculation are extracted from a $1.6'$ -wide annulus with its middle radius corresponding to the projected off-center distance of HS 1700+6416; the horizontal line represents the best-fit intensity of the data, excluding the $\pm 45^\circ$ pie around the direction $[75^\circ$ or 255° (East from North)] from the center of the considered cluster (Cluster A or B) to the center of the other one. Because HS 1700+6416 is considerably closer to Cluster A than to Cluster B, the best-fit average intensity around the former is greater than that around the latter. For the same reason, the peak (due to Cluster A) in the right panel is higher than that (due to Cluster B) in the left panel.

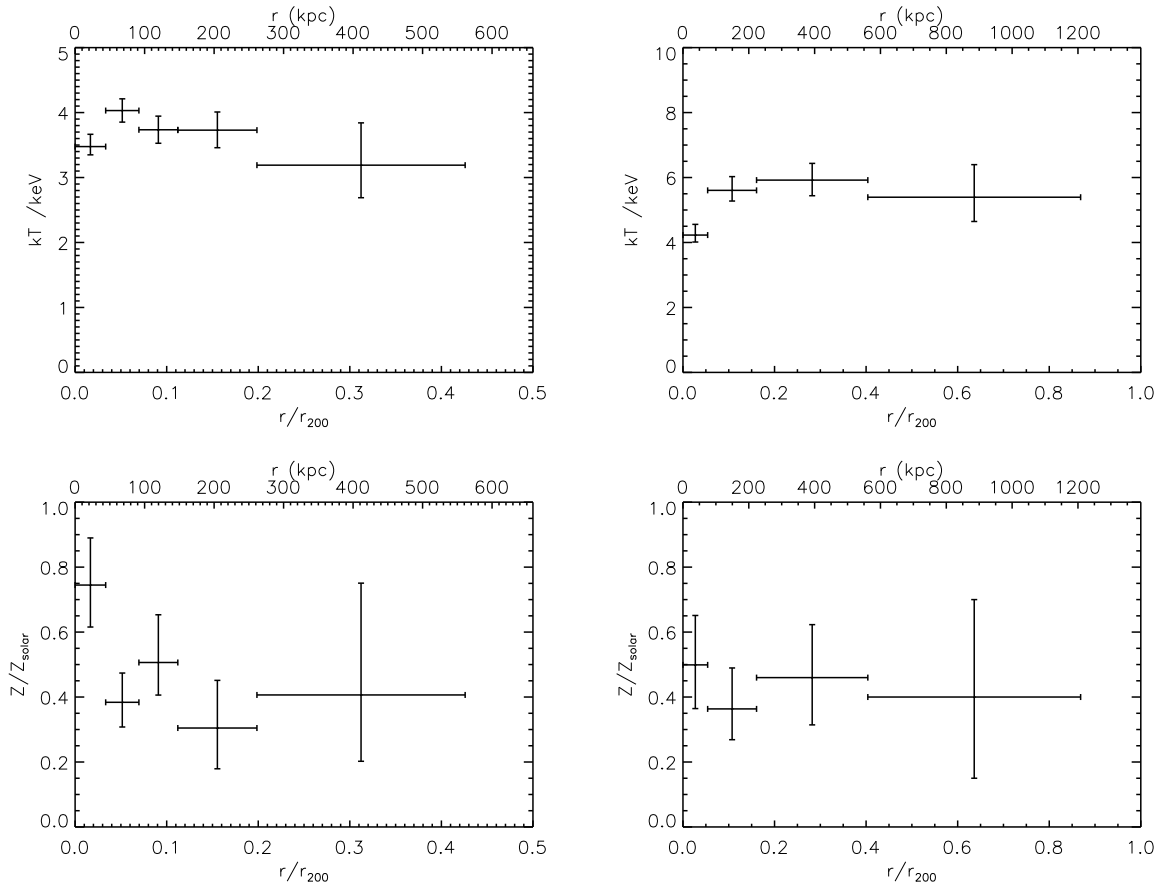


Figure 6. Temperature (upper panels) and metallicity (lower panels) for Clusters A (left) and B (right).

lations (Arnaud, Pointecouteau & Pratt 2005). The results are also included in Table 2.

3.3 Projected radial distributions of the diffuse X-ray emission

Figs. 7 and 8 present the projected radial distributions of the diffuse X-ray emission around the centers of the two clusters. The construction of the distributions for each cluster uses only the data in the half of the circle (with the projected radius $r = 1.5r_{200}$) away from the other cluster [e.g., between 165° and 345° (East from North) for Cluster A]. The distributions appear consistent in the two data sets, when viewed separately (§ 2). We fit the S band intensity profiles [panel (a) in each of the two figures] with the standard β -model of the form (Cavaliere & Fusco-Femiano 1976):

$$I = I_o \left(1 + \frac{r^2}{r_c^2} \right)^{1/2-3\beta}. \quad (1)$$

The best-fit parameters are included in Table 2. The model typically gives a good characterization of a relaxed cluster. But for Cluster A, there are clear systematic deviations of the observed profiles from the model at outer radii $r/r_{200} \sim 1$. Excluding the six consecutive data points above the model curve between $r/r_{200} = 0.9 - 1.1$, the fit improves significantly ($\chi^2/d.o.f. = 59/30$); the fitted model parameters also change significantly. Here we have accounted for only statistical counting statistics, not the discreteness of undetected sources in the field, which is likely an important source of

uncertainties. Indeed, the profiles in the H band [panel (c)] are more structured, as they are subject to more effects due to the discreteness and cosmic variance of sources just below our detection threshold. Furthermore, the X-ray intensity in the H band also depends more sensitively on the ICM temperature (hence its variation) than in the S band. Therefore, we do not present the β model fitting results for the H band here.

To assess the radial extent of the cluster emission, we use the accumulated significance distribution of the S band emission above the local background, which is χ^2 -fitted in the $r/r_{200} = 1.2 - 1.5$ range for each cluster (Figs. 7b or 8b). The use of this accumulated excess significance distribution minimizes the effect of fluctuations, which depend on the binning of the data in constructing an intensity profile. If the 2σ significance of the emission excess is considered as a threshold, we then find that the extents of Clusters A and B are about 0.9 and $1.1r_{200}$, respectively (Figs. 7b or 8b). These are likely conservative estimates of the actual extents. One indication for this is that the accumulated significance still decreases *monotonically* with the increasing radius beyond the above radii, down to the $\sim 1\sigma$ significance level (Figs. 7b or 8b). Our adopted local background may also be an over-estimate, because the $r/r_{200} = 1.2 - 1.5$ range could be contaminated by the cluster emission. Accounting for these factors, the actual extents of the emission excess are likely to be $\gtrsim 1$ and $1.1r_{200}$ for Clusters A and B, respectively. This conclusion is consistent with the radial distributions of the X-ray emission hardness ratio, $(H-S)/(H+S)$, as shown in Figs. 7d and 8d. The softening of the X-ray emission

with the decreasing radius is primarily due to the increasing contribution from the clusters, relative to the local sky background. The hardness ratio seems to be systematically below the average value of the local background for the entire radial range up to ~ 1.1 (or 1.2) r_{200} for Cluster A (or B).

4 DISCUSSION

The results presented in the last section represent the direct measurements or characterizations that we obtain with the *Chandra* data. We now proceed to extend these results by incorporating additional assumptions.

4.1 Radial density profiles of the hot intracluster medium

We have shown in § 3 that the morphology of the diffuse X-ray emission from the clusters are consistent with being azimuthally symmetric, at least away from the core regions. Thus it may be reasonable to assume an approximate spherical symmetry to infer the de-projected radial profile of the ICM electron density as a function of the physical radius r for each cluster. The S band intensity is insensitive to the plasma temperature (e.g., changing by only about 6 percent for a temperature range of 1.5–8.0 keV). We can thus first convert the intensity into an APEC emission measure, and then calculate the density profile. We do this for both clusters in the directions away from the overlapping region. The resultant density profiles are shown in Fig. 9. The average background level outside $1.2r_{200}$ (shown by the horizontal line in Figs. 7 and 8) is subtracted. Table 2 includes the integrated column densities of the hot ICM along the sightline toward HS 1700+6416.

Based on the spatially resolved temperature and density profiles (Figs. 6 and 9), we further conduct the hydrostatic mass analysis. We follow the procedure of Schmidt & Allen (2007), in which the total mass profile is assumed to be an NFW profile (Navarro, Frenk & White 1997) and the density profile is used to predict the temperatures in the annuli around each cluster, assuming hydrostatic equilibrium. The best-fit mass profile corresponds to the predicted temperature profile which matches the observed one best. The method avoids the need to use parametric fitting functions for the temperature and density profiles and the need to extrapolate them out to r_{200} , which could lead to large uncertainties in the priors (Allen et al. 2008). We find that both clusters are well fit by the NFW profile, and the resultant M_{200} and r_{200} values are completely consistent with those obtained from the scaling relations (§ 3.2).

4.2 Radial entropy profiles

The entropy profile of a cluster can provide direct information about the heating process of the ICM, especially the effect due to galactic mechanical energy feedbacks. But as shown in § 3, we cannot measure the ICM temperature at the largest radii, where cluster emission is detected, because of the limited counting statistics. If, however, we introduce a prior by assuming the universal pressure profile of Arnaud et al. (2010) to hold, we can then use our density profile to infer the temperature profile and thus the entropy profile. Note that the clusters studied in Arnaud et al. (2010) are all at redshift below 0.2, so we only investigate Cluster A here as the uncertainties in extrapolating out to the much higher redshift of $z=0.45$ are unknown.

The de-projected temperature profile, $kT = P/n_e$, can be inferred from the universal pressure profile and the de-projected density profile that we have measured, while the de-projected entropy profile can be estimated from

$$K = P/n_e^{5/3}. \quad (2)$$

Fig. 10 shows the inferred entropy profile for the cluster. Note that the error bars are derived from the errors in the density profile, and are underestimates because the uncertainty in the pressure profile is not accounted for. We compare this crude entropy profile to the power law prediction of purely gravitational hierarchical structure formation from Voit, Kay & Bryan (2005). We see that there is a central excess in entropy within $0.5r_{200}$, as has been found for samples of nearby clusters using *XMM-Newton* (Pratt et al. 2010) and *Suzaku* observations (Walker et al. 2013). Eckert et al. (2013) have also found the same central entropy excess by combining stacked *ROSAT* density profile with stacked Planck pressure profiles. Outside of $0.5r_{200}$ the scatter is large due to the uncertainties in the density de-projection. Nevertheless, the points seem to lie systematically below the baseline entropy profile. These findings suggest that the non-gravitational feedback must be important in the inner regions, while the ICM in outer regions near the virial radii may not be hydrostatic and/or ionization equilibrium and may be rather clumpy and multi-phased.

5 SUMMARY

We have conducted a detailed analysis of the *Chandra* observations of the two foreground clusters of HS 1700+6416: Abell 2246 (Cluster A) and GMBCG J255.34805+64.23661 (B). Table 2 includes the key parameters of the clusters, measured or inferred from the present work. We summarize our main results and conclusions in the following:

- Spatially, the two clusters are well resolved in the observations. In particular, the X-ray emission is found to be centered on a red early-type galaxy in each of the clusters. Whereas Cluster A appears well relaxed morphologically, the core of Cluster B is strongly elongated, probably as a result of a recent subcluster merger. The X-ray morphology of the two clusters at the impact distances of HS 1700+6416 is consistent with being azimuthally symmetric.
- Spectrally, a cool core is detected in each of the two clusters. Cluster A also shows a significant abundance enhancement in the core. Outside the cores, the ICM has a mean metal abundance of ~ 0.4 solar and a mean temperature of ~ 4.0 keV for Cluster A (or 5.5 keV for Cluster B). We have estimated the gravitational masses and the virial radii of the clusters from the ICM temperatures.
- Each of the two clusters shows significant X-ray emission extending to about $r \sim r_{200}$. Assuming a spherical symmetry of the ICM, we have obtained its radial density and temperature distributions for each cluster. By adopting a “universal” pressure profile, we have further shown that the radial entropy distribution of Cluster A is substantially flatter than what might be expected from purely gravitational hierarchical structure formation, suggesting the importance of galactic feedback in cluster inner regions and non-equilibrium of the ICM in outer regions.

The above results and conclusions represent an essential step to characterize the thermal, chemical, and dynamic states of the clusters. In particular, we can now estimate the density and temperature properties of the hot ICM along the sightline of HS

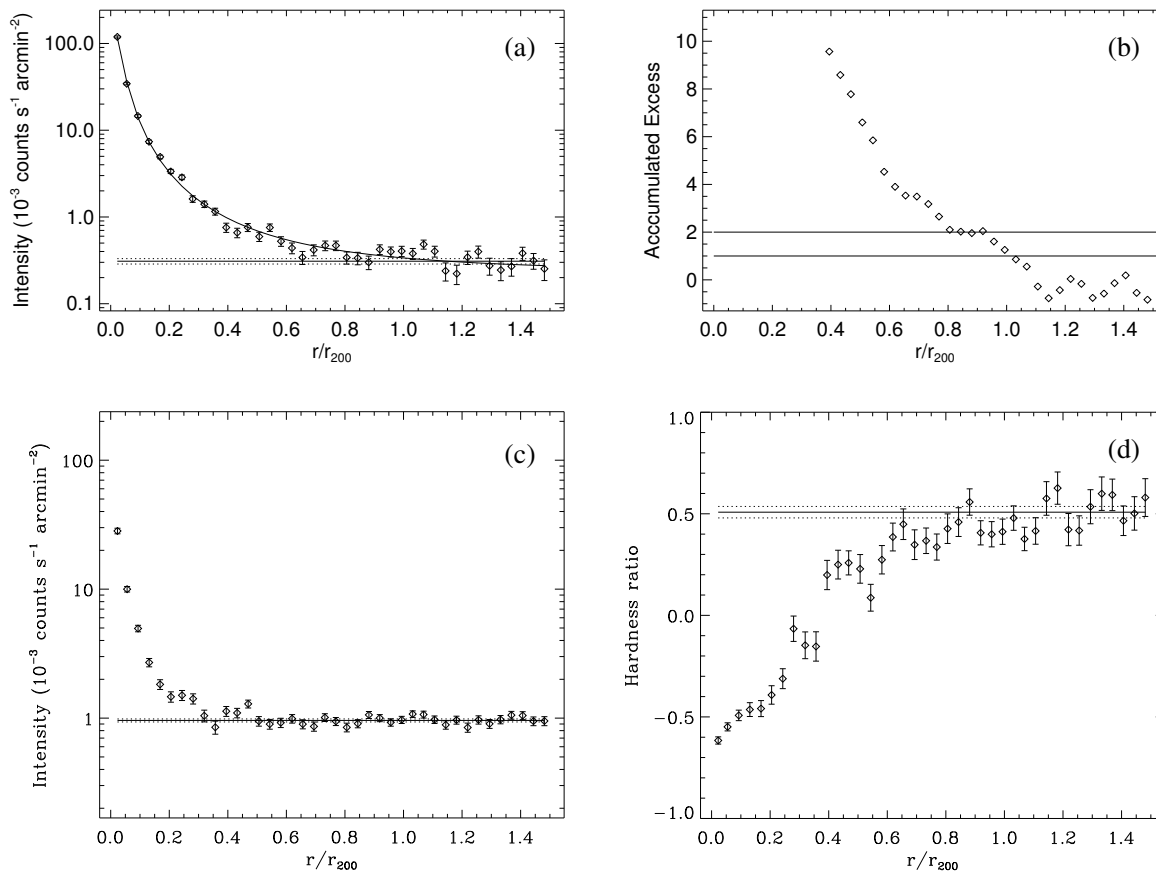


Figure 7. Projected radial distributions of the diffuse X-ray emission from Clusters A: the intensity in the S band (a) and its accumulated significance (the ratio of the accumulated intensity to its error in units of σ) above the local background; the intensity in the H band (c) and the hardness ratio of the intensities in the two bands (d). The horizontal solid (dotted) lines in the panels (a), (c) and (d) mark the local background ($\pm 1\sigma$ uncertainties) estimated with the data in the $r/r_{200} = 1.2 - 1.5$ range. The two horizontal solid lines in the panel (b) mark the 1- and 2- σ significance levels. The significance is accumulated inward from $r/r_{200} = 1.5$.

1700+6416 through the two clusters at the impact distances of 0.36 and $0.8r_{200}$.

With the upcoming *HST*/COS observations along the HS 1700+6416 sightline, we will be able to cross-correlate the properties determined from the UV absorption lines with the X-ray properties of the clusters. The *HST*/COS absorption line spectroscopy is well-suited for investigating the warm phase of the ICM, reaching column density limits of $\sim 10^{12} \text{ cm}^{-2}$ for HI and $\sim 10^{13.5} \text{ cm}^{-2}$ for OVI and to simultaneously explore other multiple transitions from a wide range of atoms/ions. The OVI doublet, in particular, is sensitive to the so-called transition temperature gas at $\sim 10^5 \text{ K}$ and is hence ideal for studying the interplay between warm and hot gas components. The combination of the lines, in terms of their column densities and velocity centroids/widths, can give powerful diagnostics of the absorbers and their relationship to the surrounding hot ICM (e.g., Tripp et al. 2008). Therefore, we will be able to examine the thermal, chemical, ionization, and kinematic properties as well as the baryon content of the multiphase ICM. Two additional pairs of FUV-bright QSO/clusters pairs at similar redshifts have been proved for COS observations. These studies will nicely complement the existing *HST*/COS observations of the very nearby Virgo cluster, although they do not allow for access to the OVI doublet (Yoon et al. 2012). 25 Ly- α absorbers ($N_{\text{HI}} \gtrsim 10^{13.1-15.4} \text{ cm}^{-2}$) are

detected toward 9 QSO sight-lines. It is concluded that the warm gas covering fraction ($\sim 100\%$ for $N_{\text{HI}} = 10^{13.1} \text{ cm}^{-2}$) is in agreement with cosmological simulations. Comparisons of the results will then provide statistical insights into the ICM/CGM properties and their dependence on various cluster properties and impact parameters.

ACKNOWLEDGMENTS

We thank the anonymous referee for valuable comments that led to an improved presentation of the paper. QDW thanks the Institute of Astronomy for the hospitality and the award of a Raymond and Beverley Sackler Distinguished Visitor fellowship. The research is also partly supported by NASA and CXC via the grants NNX12AI48G and TM3-14006X.

APPENDIX A: DISCRETE X-RAY SOURCE DETECTION

We search for X-ray sources in the S, H, and B broad bands. A combination of source detection algorithms are applied: wavelet, sliding-box, and maximum likelihood centroid fitting (Wang 2004). Our final source list contains sources with local false detection

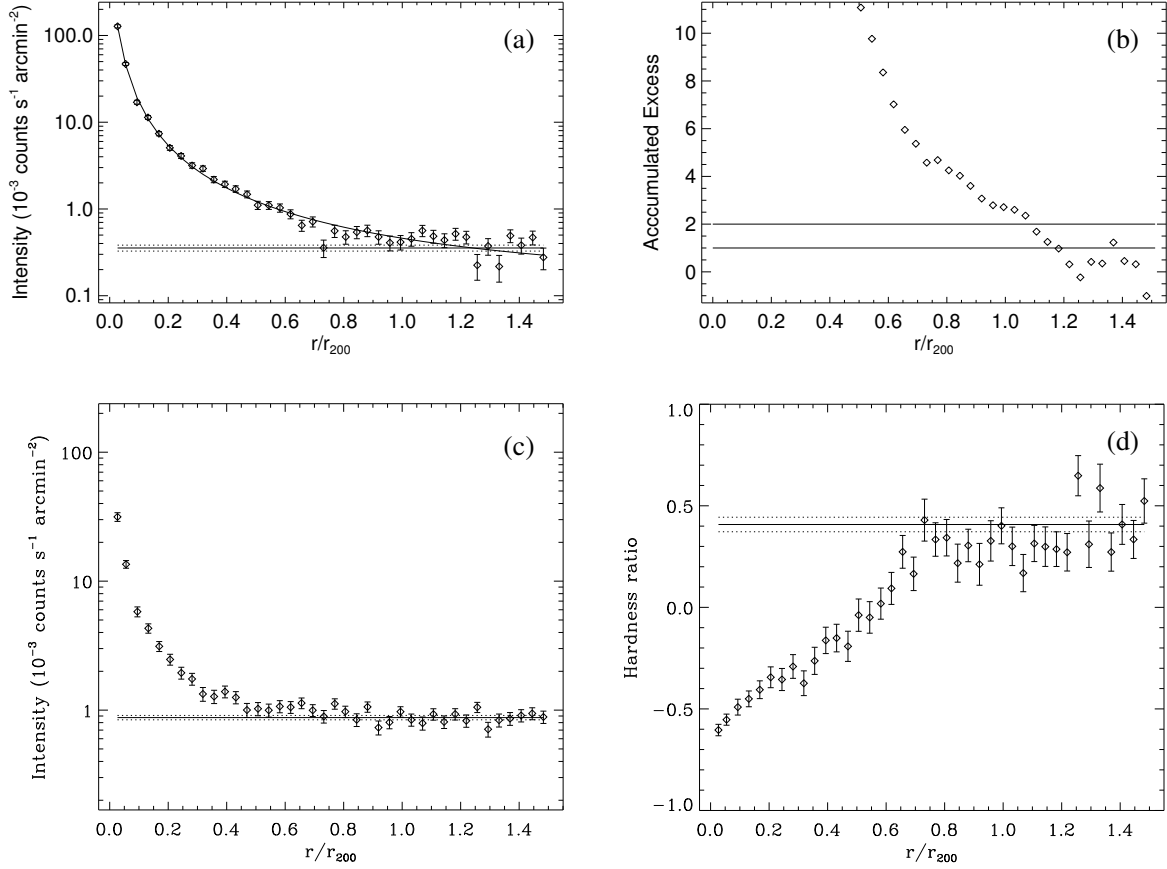


Figure 8. Same as Fig. 7, but for Clusters B.

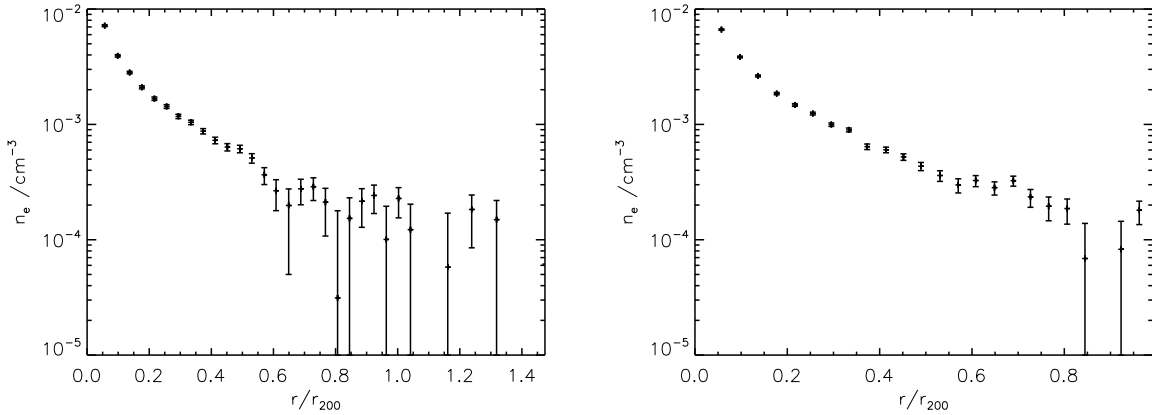


Figure 9. De-projected electron density profiles. The rest is the same as in Fig. 6.

probability less than 10^{-6} (due to the Poisson fluctuation above the local sky background). The source detection, though optimized for point-like sources, may include strong peaks of diffuse X-ray emission, chiefly associated with the centers of the clusters.

Table A1 lists our detected sources. Listed parameters of the sources are defined in the note to the table. The conversion from a count rate to an unabsorbed energy flux depends on the source spectrum and foreground absorption. A characteristic value of the con-

version is 8×10^{-12} ($\text{erg cm}^{-2} \text{s}^{-1}$)/(counts s^{-1}) in the B band for a power law spectrum of photon index 2 and an absorbing-gas column density $N_H \sim 1 \times 10^{21} \text{ cm}^{-2}$ (assuming the solar abundances). This conversion should be a good approximation (within a factor of 2) for $\lesssim 3 \times 10^{21} \text{ cm}^{-2}$.

The hardness ratios, compared with spectral models (Fig. A1), may be used to characterize the X-ray spectral properties of the sources. Of course, the spectrum of a source can be more compli-

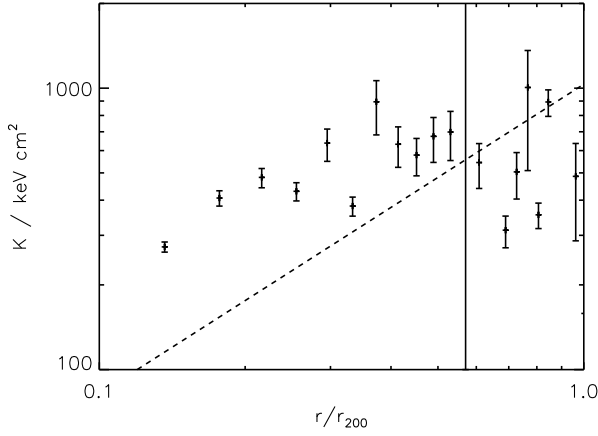


Figure 10. Entropy profile for Cluster A, derived from the de-projected density profile in Fig. 9 and the universal pressure profile of Arnaud et al. (2010). The dashed line shows the theoretical power law relation for purely gravitational hierarchical structure formation from Voit, Kay & Bryan (2005).

cated and cannot be adequately characterized by a simple power law or an optical thermal plasma model as plotted in Fig. A1; for example, a two-component model consisting of a power law plus a thermal plasma may explain those sources located below the model curves in the $HR = -0.4$ to 0.0 range. In addition, the spectrum of a source could also change substantially from one observation to another; a good example is HS 1700+6416 (#94 in Table A1), the intrinsic absorption of which varies on order of 10^{22} cm^{-2} (Lanzuisi et al. 2012).

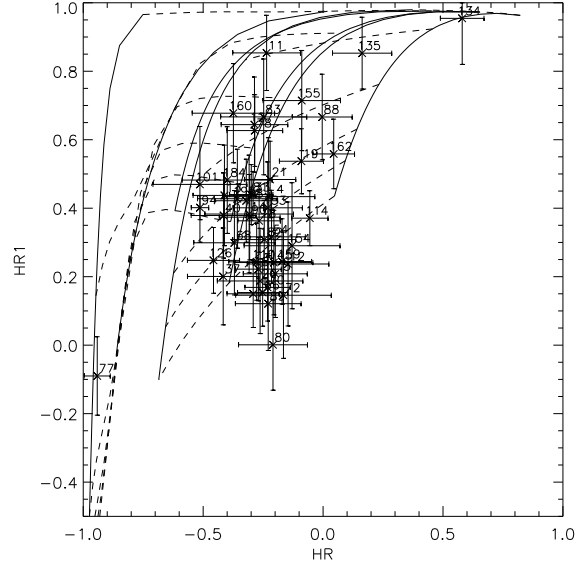


Figure A1. Color-color diagram of X-ray sources with their generic numbers (Table A1) labeled. The hardness ratios (HR and HR1) are defined in the note to Table A1, and the error bars represent 1σ uncertainties. Also included in the plot are hardness-ratio models: the solid thick curves are for the power-law model with photon index equal to 3, 2, and 1, whereas the solid thin curves are for the thermal plasma with a temperature equal to 0.3, 1, 2, and 4 keV, from left to right. The absorbing gas column densities are 1, 10, 20, 40, 100, and $300 \times 10^{20} \text{ cm}^{-2}$ (dashed curves from bottom to top)

Table A1. *Chandra* Source List

Source (1)	CXOU Name (2)	δ_x (") (3)	CR (cts ks ⁻¹) (4)	HR (5)	HR1 (6)	Flag (7)
1	J165916.79+640629.9	3.5	0.76 ± 0.14	–	0.10 ± 0.19	S
2	J165918.70+640715.0	3.8	0.38 ± 0.11	–	–	S
3	J165928.85+640551.1	2.9	1.64 ± 0.16	-0.20 ± 0.13	0.21 ± 0.13	B
4	J165930.94+640631.9	2.7	0.85 ± 0.12	-0.23 ± 0.19	0.43 ± 0.17	B
5	J165931.04+640816.2	3.2	0.12 ± 0.07	–	–	S
6	J165934.84+640955.5	2.3	0.18 ± 0.06	–	–	B
7	J165939.79+640805.0	2.5	0.21 ± 0.06	–	–	B
8	J165939.93+640642.9	3.1	0.19 ± 0.07	–	–	S
9	J165941.23+640533.6	2.7	0.30 ± 0.10	–	–	S
10	J165942.46+640728.6	2.2	0.35 ± 0.08	–	–	B

...

Complete table published online

The definition of the bands: S=S1+S2, H=H1+H2, and B=S+H. Column (1): Generic source number. (2): *Chandra* X-ray Observatory (unregistered) source name, following the *Chandra* naming convention and the IAU Recommendation for Nomenclature (e.g., <http://cdsweb.u-strasbg.fr/iau-spec.html>). (3): Position uncertainty (1σ) calculated from the maximum likelihood centroiding and an approximate off-axis angle (r) dependent systematic error $0''.2 + 1''.4(r/8')^2$ (an approximation to Fig. 4 of Feigelson et al. (2002)), which are added in quadrature. (4): On-axis source broad-band count rate — the sum of the exposure-corrected count rates in the four bands and are estimated within (and corrected for) the 70% energy-encircled radius of the point spread function, depending on the off-axis angle. (5-6): The hardness ratios defined as $HR = (H - S2)/(H + S2)$, and $HR1 = (S2 - S1)/S$, listed only for values with uncertainties less than 0.2. (7): The label “B”, “S”, or “H” marks the band in which a source is detected with the most accurate position that is adopted in Column (2).

REFERENCES

- Allen S. W., Rapetti D. A., Schmidt R. W., Ebeling H., Morris R. G., Fabian A. C., 2008, *MNRAS*, 383, 879
- Anders E., Grevesse N., 1989, *Geochim. Cosmochim. Acta*, 53, 197
- Arnaud M., Pointecouteau E., Pratt G. W., 2005, *A&A*, 441, 893
- Arnaud M., Pratt G. W., Piffaretti R., Böhringer H., Croston J. H., Pointecouteau E., 2010, *A&A*, 517, A92
- Bonamente M., Landry D., Maughan B., Giles P., Joy M., Nevalainen J., 2013, *MNRAS*, 428, 2812
- Carlstrom J. E., Holder G. P., Reese E. D., 2002, *ARA&A*, 40, 643
- Cavaliere A., Fusco-Femiano R., 1976, *A&A*, 49, 137
- Digby-North J. A. et al., 2010, *MNRAS*, 407, 846
- Eckert D., Molendi S., Vazza F., Ettori S., Paltani S., 2013, *A&A*, 551, A22
- Eckert D. et al., 2012, *A&A*, 541, A57
- Ettori S., Balestra I., 2009, *A&A*, 496, 343
- Feigelson E. D., Broos P., Gaffney, III J. A., Garmire G., Hillenbrand L. A., Pravdo S. H., Townsley L., Tsuboi Y., 2002, *ApJ*, 574, 258
- George M. R., Fabian A. C., Sanders J. S., Young A. J., Russell H. R., 2009, *MNRAS*, 395, 657
- Hickox R. C., Markevitch M., 2006, *ApJ*, 645, 95
- Hoshino A. et al., 2010, *PASJ*, 62, 371
- Just D. W., Brandt W. N., Shemmer O., Steffen A. T., Schneider D. P., Chartas G., Garmire G. P., 2007, *ApJ*, 665, 1004
- Kalberla P. M. W., Burton W. B., Hartmann D., Arnal E. M., Bajaja E., Morras R., Pöppel W. G. L., 2005, *A&A*, 440, 775
- Koutroumpa D., Lallement R., Kharchenko V., Dalgarno A., Pepino R., Izmodenov V., Quémerais E., 2006, *A&A*, 460, 289
- Lanzuisi G., Giustini M., Cappi M., Dadina M., Malaguti G., Vignali C., Chartas G., 2012, *A&A*, 544, A2
- Lu Z., Wang Q. D., 2011, *MNRAS*, 413, 347
- Maughan B. J., Jones C., Forman W., Van Speybroeck L., 2008, *ApJS*, 174, 117
- Molnar S. M., Hearn N., Haiman Z., Bryan G., Evrard A. E., Lake G., 2009, *ApJ*, 696, 1640
- Navarro J. F., Frenk C. S., White S. D. M., 1997, *ApJ*, 490, 493
- Pratt G. W. et al., 2010, *A&A*, 511, A85
- Reimers D., Toussaint F., Hagen H.-J., Hippelein H., Meisenheimer K., 1997, *A&A*, 326, 489
- Roncarelli M., Ettori S., Dolag K., Moscardini L., Borgani S., Murante G., 2006, *MNRAS*, 373, 1339
- Schmidt R. W., Allen S. W., 2007, *MNRAS*, 379, 209
- Simionescu A. et al., 2011, *Science*, 331, 1576
- Tripp T. M., Sembach K. R., Bowen D. V., Savage B. D., Jenkins E. B., Lehner N., Richter P., 2008, *ApJS*, 177, 39
- Voit G. M., Kay S. T., Bryan G. L., 2005, *MNRAS*, 364, 909
- Walker S. A., Fabian A. C., Sanders J. S., Simionescu A., Tawara Y., 2013, *MNRAS*, 432, 554
- Wang Q. D., 2004, *ApJ*, 612, 159
- Yoon J. H., Putman M. E., 2013, *ApJ*, 772, L29
- Yoon J. H., Putman M. E., Thom C., Chen H.-W., Bryan G. L., 2012, *ApJ*, 754, 84